How to cite: Angew. Chem. Int. Ed. 2024, e202417244
doi.org/10.1002/anie.202417244

Organic Solar Cells

Rebuilding Peripheral F, Cl, Br Footprints on Acceptors Enables Binary Organic Photovoltaic Efficiency Exceeding 19.7 %

Xiangjian Cao[+], Peiran Wang[+], Xinyuan Jia, Wenkai Zhao, Hongbin Chen, Zheng Xiao, Jiaqi Li, Xingqi Bi, Zhaoyang Yao, Yaxiao Guo, Guankui Long, Chenxi Li, Xiangjian Wan, and Yongsheng Chen**

Abstract: Given homomorphic fluorine (F), chlorine (Cl) and bromine (Br) atoms are featured with gradually enlarged polarizability/atomic radius but decreased electronegativity, the rational screen of halogen species and locations on small molecular acceptors (SMAs) is quite essential for acquiring desirable molecular packing to boost efficiency of organic solar cells (OSCs). Herein, three isomeric SMAs (CH–F, CH–C and CH–B) are constructed by delicately rebuilding peripheral F, Cl, Br footprints on both central and end units. Such a re-permutation of peripheral halogens could not only maintain the structural symmetry of SMAs to the maximum, but also acquire extra asymmetric benefits of enhanced dipole moment and intramolecular charge transfer, etc. Moreover, central brominating enhances molecular crystallinity of CH–B without introducing undesirable steric hindrance on end groups, thus rendering a better balance between high crystallization and domain size control in PM6:CH–B blend. Further benefitting from the large dielectric constant, small exciton binding energy, optimized molecular packing and great electron transfer integral, CH–B affords the first class binary OSC efficiency of 19.78 %, moreover, the highest efficiency of 18.35 % thus far when increasing active layer thickness to ~300 nm. Our successful screening in rebuilding peripheral halogen footprints provides the valuable insight into further rational design of SMAs for record-breaking OSCs.

Introduction

The successively increased power conversion efficiency (PCE) of organic solar cells (OSCs) in the past few years mainly benefits from the synchronized exploration of innovative small molecular acceptors (SMAs).[1] In order to overcome the intrinsic loose/disorder accumulation of organic materials, the strategy of two-dimensional (2D) conjugation extension of central units along with sufficient peripheral halogenation has been developed to enhance molecular packing strength and crystalline ordering, thus accelerating exciton diffusion and charge transfer/transport.[2] Especially, the 2D conjugation expanded central units could usually provide extra and sufficient halogenating sites besides end units. This makes it possible to delicately tune molecular packing modes and crystallization through regulating halogen species, amount and spatial locations at the full periphery of molecular skeletons rather than only the end units.[3] To be specific, besides the great effects on energy level and absorption of SMAs, peripheral halogens could also (1) construct multiple secondary interactions (X–H, X–S, X–π) to enhance intermolecular packing strength and induce better crystalline ordering;[4] (2) increase molecular isotropic polarizability and relative dielectric constant (ε_r), thus reduce energy barrier for charge separation (similar to exciton binding energy E_b) of SMAs further.[5]

Note that the homomorphic fluorine (F), chlorine (Cl), bromine (Br), and iodine (I) atoms are featured with gradually enlarged polarizability/atomic radius but decreased electronegativity (Figure 1a). Among them, F/Cl have been widely employed due to their relatively large electronegativity and small steric hindrance.[6] As regards to Br/I, although their large atomic radius usually induce the nonnegligible steric hindrance, some unique advantages of quite easy polarization and high crystallinity are still rendered.[7] Therefore, for a molecular platform that owns up to eight available halogenation sites (like CH-series SMAs),[8] the delicate construction of peripheral halogenation footprint should be crucially important (Figure 1b and

[*] X. Cao,[+] P. Wang,[+] X. Jia, H. Chen, Z. Xiao, J. Li, X. Bi, Z. Yao, C. Li, X. Wan, Y. Chen
State Key Laboratory and Institute of Elemento-Organic Chemistry, Frontiers Science Center for New Organic Matter, The Centre of Nanoscale Science and Technology and Key Laboratory of Functional Polymer Materials, Institute of Polymer Chemistry, Renewable Energy Conversion and Storage Center (RECAST), College of Chemistry, Nankai University, Tianjin, 300071, China
E-mails:
E-mail: yschen99@nankai.edu.cn
zyao@nankai.edu.cn
Y. Guo
State Key Laboratory of Separation Membranes and Membrane Processes, School of Chemistry, Tiangong University, Tianjin 300387, China
P. Wang,[+] W. Zhao, G. Long
School of Materials Science and Engineering, National Institute for Advanced Materials, Renewable Energy Conversion and Storage Center (RECAST), Nankai University, Tianjin, 300350, China
[+] These authors contributed equally: Xiangjian Cao, Peiran Wang

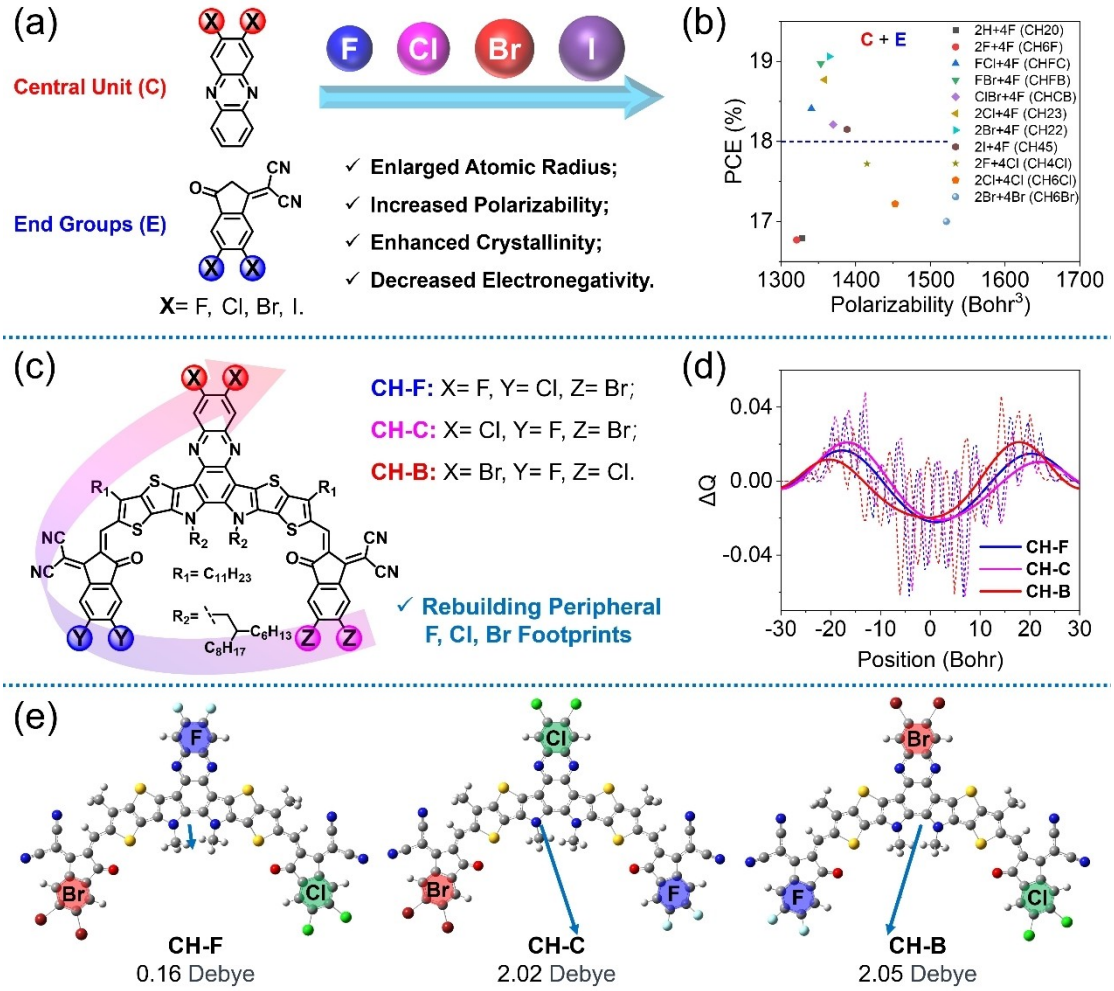

Figure 1. (a) Chemical structures of central and end units, with properties evolution from fluorine to iodine. (b) PCE variation affected by different peripheral halogen combinations. Referring to **Table S1** for the details. (c) Chemical structures of CH–F, CH–C and CH–B. (d) Theoretically calculated frontier orbital charge density differences (ΔQ). (e) Calculated dipole moments and orientation of CH–F, CH–C and CH–B.

Table S1). For instance, the strong crystalline Br with more electronegative F or Cl atoms, together with balancing their spatial locations, could fine-tune the crystallization/packing ordering of SMAs and micro-morphology of active layers. Moreover, such a footprint rebuilding of peripheral halogen could not only keep the structural symmetry of SMAs, but also acquire extra asymmetric benefits of enhanced dipole moment and intramolecular charge transfer, etc.[9]

Bearing above thoughts in mind, three highly efficient isomeric SMAs of CH–F, CH–C and CH–B have been designed and synthesized by rebuilding peripheral F, Cl, Br footprints on a 2D conjugation extended molecular platform (Figure 1c), with the aim of delicately tuning the photophysical property of SMAs at both single-molecular and aggregated levels. The up to eight available halogenation sites on such a 2D platform firstly make it possible to build unique peripheral halogen footprint for each SMAs. Thus, a systematic investigation has been carried and revealed that central brominating could enhance molecular crystallinity of SMAs without introducing undesirable steric hindrance on end groups, thus rendering the enlarged ε_r, decreased E_b, optimized molecular packing and more suitable fibrillary morphology. As a consequence, CH–B with central brominating affords an excellent binary OSC efficiency of 19.78 %. Moreover, the highest efficiency of 18.35 % thus far has been reached for the device with the active layer thickness up to ~300 nm. Our work paves a new avenue for constructing record-breaking OSCs, by delicately building unique peripheral halogen footprints on 2D conjugation expanded SMAs.

Results and Discussions

Physicochemical Properties

As discussed above, peripheral halogen re-permutation is expected to exert negligible effects on molecular planarity of SMAs. This has been confirmed by the density functional theory (DFT) simulations of molecular geometries. As displayed in Figure 1d and Figure S1, a desirable acceptor-donor-acceptor feature for all the three SMAs can be

indicated by the conspicuous peak-valley-peak profiles of frontier orbital charge density differences.[10] Due to the much larger electronegativity of F than Cl/Br atoms (4.0 for F, 3.0 for Cl and 2.8 for Br) and asymmetric permutation of peripheral halogens, the location of electron-donating and withdrawing centers sways and fluctuates along the molecular backbones, especially for CH–C and CH–B. Therefore, the dipole moments of CH–C (2.02 Debye) and CH–B (2.05 Debye) greatly increased with a direction from central to fluorinated end units, which is in sharp contrast to that of 0.16 Debye for CH–F (Figure 1e). Note due to the unsymmetrical nature of the molecules, the dipole moments are not either parallel or perpendicular to the main backbone of the molecules. The large dipole moment is helpful to cause more compact and ordered molecular stacking in some cases, further facilitate electron migration from central donor to electron-deficient terminals after photoexcitation.[11] As listed in Figure S2, the highly similar but slightly enlarged band gaps of 2.01 eV for CH–F, 2.02 eV for CH–C and 2.03 eV for CH–B were rendered by DFT calculations, which agrees well with the stepwise blue-shifted maximum absorption peaks from CH–F to CH–B (Figure 2a). All the three SMAs give rise to very similar molar extinction coefficient of ~2.12×10^5 M^{-1} cm^{-1} in chloroform solutions, however, gradually enlarged one from CH–F to CH–B in their neat and blended films (Figure S3). In addition, the maximum absorption peaks in solid films display an apparent red shift compared to that in chloroform solutions, with $\Delta\lambda$ of 70, 72 and 76 nm for CH–F, CH–C and CH–B, respectively (**Table S2**). Note that the clear absorption variation including molar extinction coefficient and red shift suggests that SMAs possess different molecular packing preference induced by their unique peripheral halogen footprint.[12]

Due to the isomeric structures of CH–F, CH–C and CH–B, almost the same decomposition temperatures around 326 °C were afforded (Figure 2b), exhibiting the excellent thermal stability in view of material itself. As indicated by the differential scanning calorimetry (DSC) curves in Figure 2c, CH–F, CH–C and CH–B present the exothermal peaks at 282, 293 and 298 °C, affording a melting enthalpy (ΔH_m) of 19.96, 23.65 and 28.18 J g^{-1}, respectively. The enlarged ΔH_m from CH–F to CH–B suggests the gradually stronger interaction between the adjacent molecules.[13] In

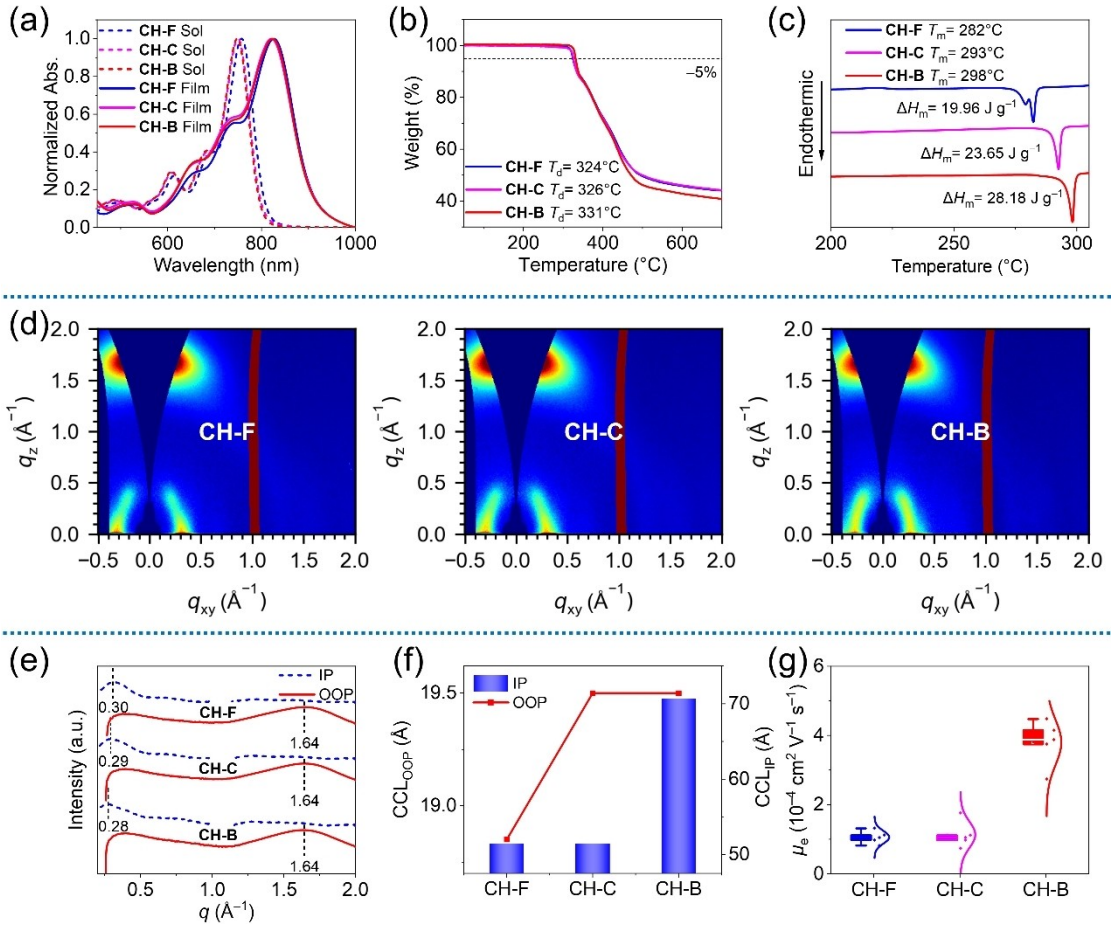

Figure 2. (a) UV/Vis spectra for CH–F, CH–C and CH–B in solutions and solid films. (b) Thermogravimetric analysis. (c) DSC curves of CH–F, CH–C and CH–B at a heating rate of 10 K min^{-1}. (d) 2D GIWAXS patterns of CH–F, CH–C and CH–B neat films. (e) Line-cut profiles of 2D GIWAXS patterns of CH–F, CH–C and CH–B neat films. (f) CCLs variation derived from GIWAXS measurements. (g) Electron mobilities of CH–F, CH–C and CH–B of neat films derived from the space-charge-limited current (SCLC) measurements.

order to further shed light on the aggregation behavior of SMAs, the grazing-incidence wide-angle X-ray scattering (GIWAXS) signals of their neat films were recorded in Figure 2d and the relevant data were listed in **Table S3**. The line-cut curves shown in Figure 2e presented obvious (010) and (100) diffraction peaks in out-of-plane (OOP) and in-plane (IP) directions, respectively, indicating a desirable face-on orientation for three SMAs.[14] Note that CH–F, CH–C and CH–B yielded almost the same π–π stacking distance of 3.83 Å, but slightly different crystal coherence lengths (CCLs) of 18.85, 19.50 and 19.50 Å, respectively, in OOP directions (Figure 2f). Moreover, CH–B also exhibit a quite larger CCL of 70.69 Å in IP direction with respect to 51.41 Å for CH–F and CH–C, indicative of the better interlayer lattice ordering in CH–B film. The enhanced molecular packing ordering of CH–B is expected to favor efficient electron transport. This is consistent with the observed larger electron mobility (μ_e) for CH–B films (Figure 2g and S4).[15]

As discussed above, the fluorinated terminals have contributed to the larger dipole moments for CH–C and CH–B. Moreover, the gradually enlarged ε_r could be also yielded with fluorinated terminals, being 1.73 for CH–F, 1.86 for CH–C and 2.18 for CH–B (Figure S5). Moreover, the trend of ε is roughly consistent with the refractive index measured by ellipsometry (Figure S6). As shown in Figure S7, all the three acceptors in diluted solutions show the similar exciton lifetimes (τ) of ~1.4 ns due to the isomeric and similar chemical structures. However, the slightly enlarged τ could be observed from CH–F, CH–C to CH–B solid films, which should be mainly affected by their more orderly molecular stackings. Temperature-varying photoluminescence (PL) spectra of CH–F, CH–C and CH–B films were recorded in Figure 3a–c with the aim of evaluating E_b variation caused by peripheral F, Cl, Br footprints rebuilding.[16] As illustrated in Figure 3d, the much smaller E_b of 19.7 for CH–C and 41.5 meV for CH–B have been rendered with respect to that of 96.4 meV for CH–F. Note that the absolute values of E_b are actually difficult to be indicated by temperature-varying PL, however, the relative comparison between similar samples should be reliable. Obviously, CH–C and CH–B demonstrate the reduced E_b comparing to that of CH–F, which may be determined by the following factors: (1) at the single molecular level, CH–C and CH–B show the greatly enlarged dipole moments of 2.02 and 2.05 Debye, respectively, comparing to that of 0.16 Debye for CH–F (Figure 1e); (2) at the aggregation level, the quite different molecular packing modes of three acceptors (see single crystal analysis below) should also affect the E_b significantly.[16a] Therefore, the difference in E_b for three acceptors should be induced by both molecular structure variations and different intermolecular electronic interactions. These results above also highlight that the delicately re-permuting peripheral halogen

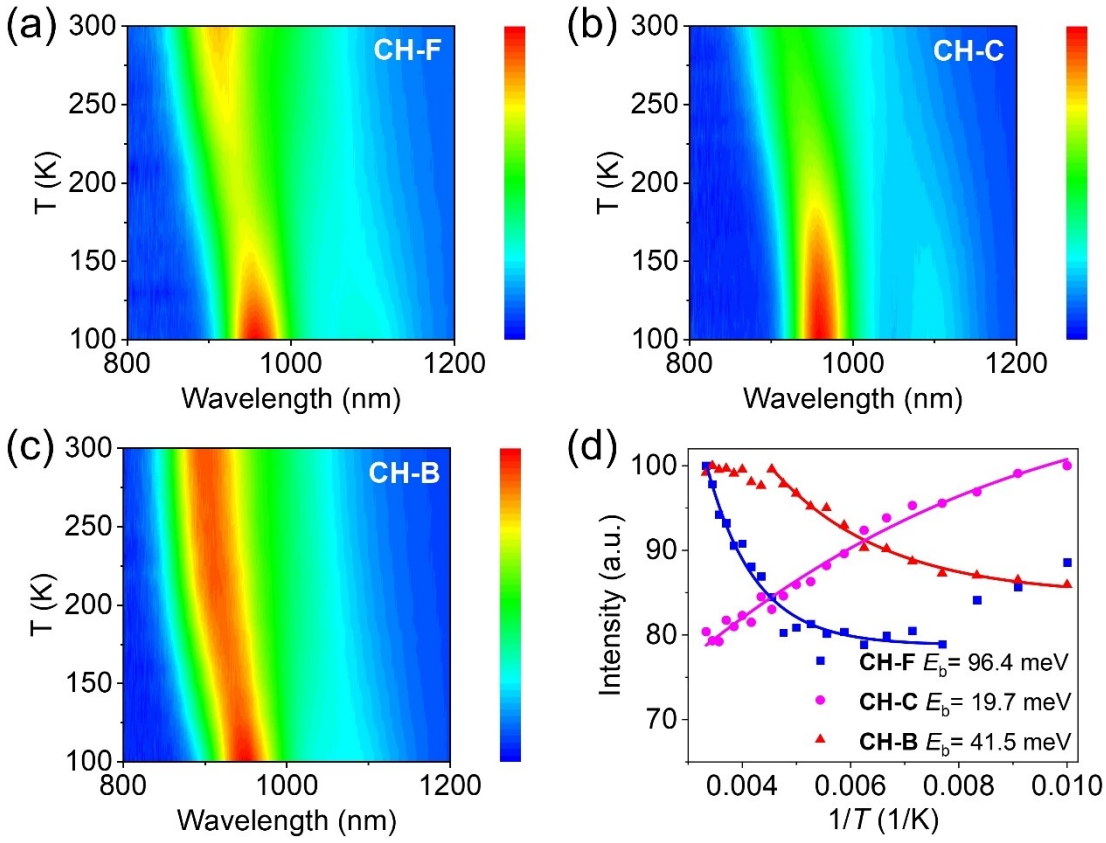

Figure 3. The temperature-dependent PL spectra of (a) CH–F, (b) CH–C and (c) CH–B in their neat films. (d) E_bs derived from the temperature dependent data of integrated intensity.

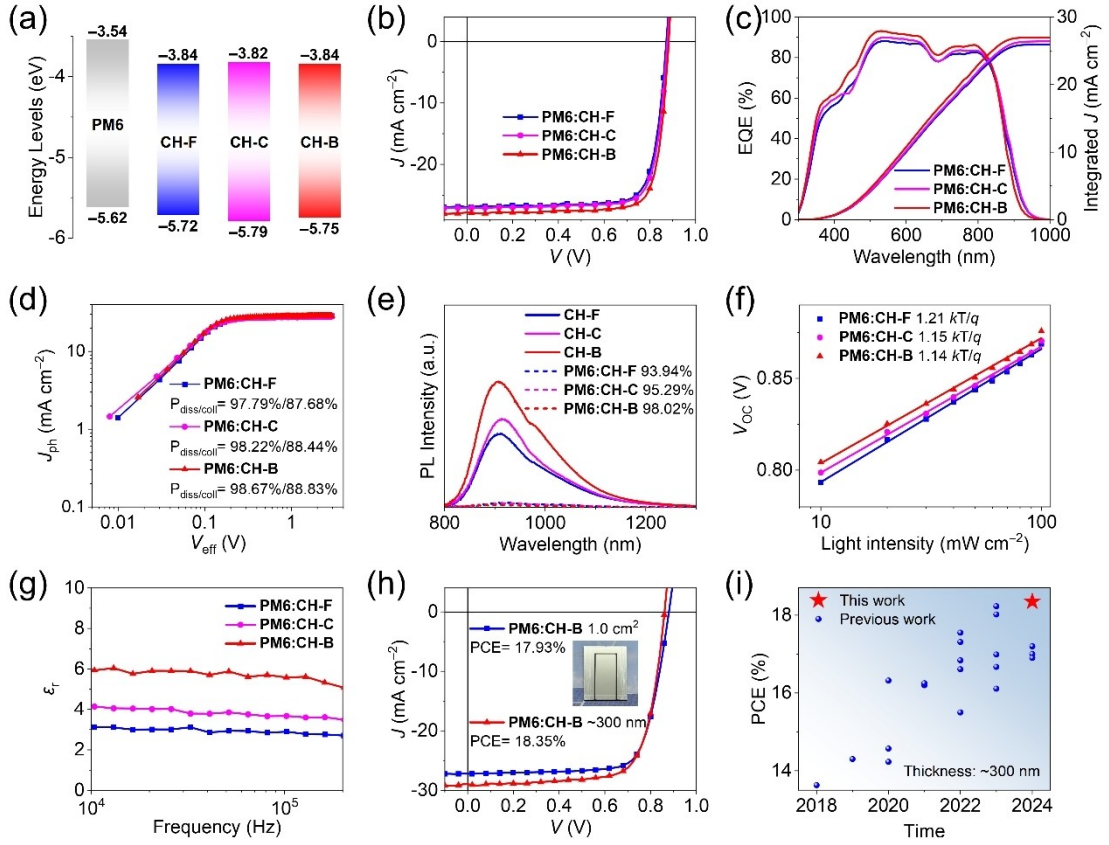

Figure 4. (a) Energy levels of PM6, CH–F, CH–C and CH–B derived from CV measurements. (b) *J*–*V* curves for champion OSCs. (c) EQE plots and integrated J_{sc} curves. (d) J_{ph} versus V_{eff} curves indicating P_{diss} and P_{coll}. (e) PL spectra of neat and blend films indicating efficiencies of PL quenching. (f) P_{light} dependence of V_{oc}. (g) ε_r as a function of frequency measured by impedance spectroscopy. (h) *J*–*V* curves for OSCs with ~300 nm active layer thickness and OSCs with 1.0 cm^2 active layer area. (i) Statistical PCE diagram of OSCs with ~300 nm active layer thickness, showing the best values achieved by this work (**Table S9**).

locations on backbones of SMAs should be an effective pathway to greatly reduce E_b of organic materials (potentially as small as inorganic semiconductors).[5b] Such a desired nature of photogenerated excitons could greatly boost the exciton dissociation even driven by a quite small driving force, and suppress the most concerned non-radiative recombination in OSCs.[17]

Photovoltaic Performances

The HOMO/LUMO energy levels of PM6,[18] (Figure S8) CH–F, CH–C and CH–B that derived from cyclic voltammetry (CV) were calculated as −5.62/−3.54, −5.72/−3.84, −5.79/−3.82 and −5.75/−3.84 eV, respectively (Figure 4a and S9). Given the well-matched energy levels and complementary absorption, we used PM6 donor to blend with three isomeric SMAs and further fabricated the OSCs with a conventional structure. The device fabrication and optimization processes were described and enumerated in Supporting Information (**Table S4–S6**). The best *J*–*V* characteristics and derived photovoltaic parameters were exhibited in Figure 4b–c and Table 1, respectively.

For CH–F-based binary OSCs, a good PCE of 18.55 % with an open-circuit voltage (V_{oc}) of 0.872 V, a short-circuit current density (J_{sc}) of 27.01 mA cm^{-2} and a fill factor (FF) of 78.74 % is delivered. After peripheral halogen repermutation, a better PCE of 18.94 % is afforded by CH–C-based devices with a slightly improved V_{oc} of 0.876 V, J_{sc} of 27.10 mA cm^{-2} and FF of 79.77 %. More excitingly, an excellent PCE of 19.78 % is further achieved by CH–B-based OSCs with a much better FF of 80.46 %, which ranks among the highest PCEs for binary OSCs. The recorded external quantum efficiency (EQE) plots in Figure 4c showed a gradually increasing trend from CH–F, CH–C to CH–B-based OSCs, yielding the integrated J_{SC}s of 25.93, 26.40 and 26.98 mA cm^{-2}, respectively. In order to disclose the underlying reasons for J_{sc} and FF improvement in CH–B-based devices, we firstly evaluated the exciton dissociation (P_{diss}) and charge collection (P_{coll}) efficiencies through measuring the dependence of photocurrent density (J_{ph}) versus effective voltage (V_{eff}). As displayed in Figure 4d, the values of P_{diss}/P_{coll} can be estimated as 97.79 %/87.68 % for CH–F, 98.22 %/88.44 % for CH–C and 98.67 %/88.83 % for CH–B-based devices. The slightly enlarged P_{diss} is consistent with the PL quenching efficiencies of 93.94 % for CH–F, 95.29 % for CH–C and 98.02 % for CH–B

Table 1: Summary of photovoltaic parameters for OSCs.[a]

Active layers	V_{oc} (V)	J_{sc} (mA cm^{-2})	Cal. J_{sc}[b] (mA cm^{-2})	FF (%)	PCE (%)
PM6:CH-F	0.872 (0.867 ± 0.003)	27.01 (26.95 ± 0.24)	25.93	78.74 (78.88 ± 0.35)	18.55 (18.42 ± 0.15)
PM6:CH-C	0.876 (0.873 ± 0.003)	27.10 (27.04 ± 0.27)	26.40	79.77 (79.11 ± 0.47)	18.94 (18.68 ± 0.18)
PM6:CH-B	0.883 (0.884 ± 0.002)	27.85 (27.70 ± 0.08)	26.98	80.46 (80.45 ± 0.14)	19.78 (19.69 ± 0.05)

[a]Average parameters derived from 15 independent OSCs (**Table S4–S6**). [b]Current densities by integrating EQE plots.

blended films (Figure 4e). By measuring the dependence of V_{oc} and J_{sc} on light intensity (Figure 4f and S10), S/(kT/q) for PM6:CH–F, PM6:CH–C and PM6:CH–B-based devices were determined to be 1.21, 1.15 and 1.14, respectively, suggesting slightly but stepwise reduced trap-assisted charge recombination.[19] Moreover, the larger charge carrier lifetimes (42 μs for PM6:CH–C and 65 μs for PM6:CH–B) and smaller charge extraction times (0.46 μs for PM6:CH–C and 0.45 μs for PM6:CH–B) can be observed from the transient photovoltage (TPV) and transient photocurrent (TPC) decay curves, comparing to that of 26 μs and 0.51 μs for PM6:CH–F, respectively (Figure S11). This indicates the superior charge transport and recombination features in PM6:CH–C and PM6:CH–B blended films. Then, the charge transport behaviors in CH–F, CH–C and CH–B-based blends were further evaluated by using the SCLC method. As shown in Figure S12, the μ_e/hole mobility (μ_h) could be determined as 4.48/2.64, 5.32/3.31 and 5.82/3.94×10^{-4} cm^2 V^{-1} s^{-1}, respectively, giving rise to the μ_e/μ_h ratios of 1.70, 1.61 and 1.48. The gradually enlarged ε_r of 2.90 for PM6:CH–F, 3.68 for PM6:CH–C and 5.58 for PM6:CH–B blends should be conducive to charge generation/migration in PM6:CH–B blends (Figure 4g and S13).[20] In addition, due to the isomeric structures of CH–F, CH–C and CH–B, similar energy losses have been achieved as well in light of their similar V_{OC}s and nearly the same absorptions (Figure S14, S15 and **Table S7**). Moreover, the three binary OSCs could maintain ~90 % of their initial PCEs after ~1500 h testing at room temperature, and PM6:CH–B-based OSC kept 92.1 % of its initial PCE after ~500 h at 65 °C, whereas the PM6:CH–F and PM6:CH–C only retained ~86 % of their initial PCEs (Figure S16). To sum up, the overall improved exciton dissociation and charge transport/recombination contribute most to the simultaneously improved J_{sc} and FF from CH–F, CH–C to CH–B-based OSCs. These results also manifest that the photovoltaic performance of OSCs could be significantly improved through constructing unique and suitable peripheral halogen footprints of SMAs using the same optimized backbone structure. This would clearly offer an effective pathway to further improve the performance of OSCs.

Given the already excellent photovoltaic performance of CH–B-based OSCs, we further investigated its thickness-dependence performance, which may determine its prospect of large-scale printing productions. Note that nearly all the high-performance OSCs were reached with a ~100 nm active layer thickness and the PCEs usually descend drastically with thickness increasing.[21] Due to the enhanced crystallinity caused by brominating and relatively good charge mobility, CH–B might be expected to behavior differently for the thickness-dependence performance. On basis of these considerations, we fabricated PM6:CH–B based OSCs with different active layer thicknesses (~200, ~300, and ~400 nm). The resulting J–V curves and EQE plots were exhibited in Figure 4h and S17, with detailed photovoltaic parameters listed in **Table S8**. The J_{sc} of OSCs improves significantly with the film thickness increasing, however, the FF declines obviously. Consequently, an ecstatic PCE of 18.35 % is yielded eventually by PM6:CH–B- based OSCs with a ~300 nm film thickness, showing the excellent tolerance of film thickness. It is worth noting that 18.35 % is the best PCE value for OSCs with thickness up to ~300 nm thus far (Figure 4i and **Table S9**). With the thickness of active layer increasing, the PCEs of resulting OSCs decreased stepwise. This is mainly caused by the more extensive trap-assisted recombination in thicker-film devices (Figure S18). Moreover, as illustrated in Figure 4h, PM6:CH–B- based OSCs with 1.0 cm^2 active area delivered a really excellent efficiency of 17.93 %, accompanied by a J_{sc} of 27.21 mA cm^{-2}, a V_{oc} of 0.880 V and an FF of 74.88 %. Both the excellent thick-film and large-area photovoltaic performances have made CH–B as a very promising candidate for large-scale applications.[22]

Morphology Analysis

As it is well known, the device performance of OSCs is associated to the nanoscale blended morphology of active layers closely. Therefore, atomic force microscopy based infrared spectroscopy (AFM-IR) was firstly employed to disclose the morphology changes after rebuilding peripheral F, Cl, Br footprints on SMAs. As displayed in Figure S19 and S20, all the three blends were characteristic of a uniform and smooth film surface, indicated by a root-mean-square roughness (R_q) of ~0.8 nm. Then, we recorded AFM-IR signals of blended films by detecting wavenumber at 2216 cm^{-1},[23] which should be the stretching vibration of C≡N bond in SMAs. As shown in Figure 5a, it is obvious that D/A interpenetrating fibrillary networks at nanoscale can be observed, especially for PM6:CH–B blend with a clearer D/A boundary. Additionally, transmission electron

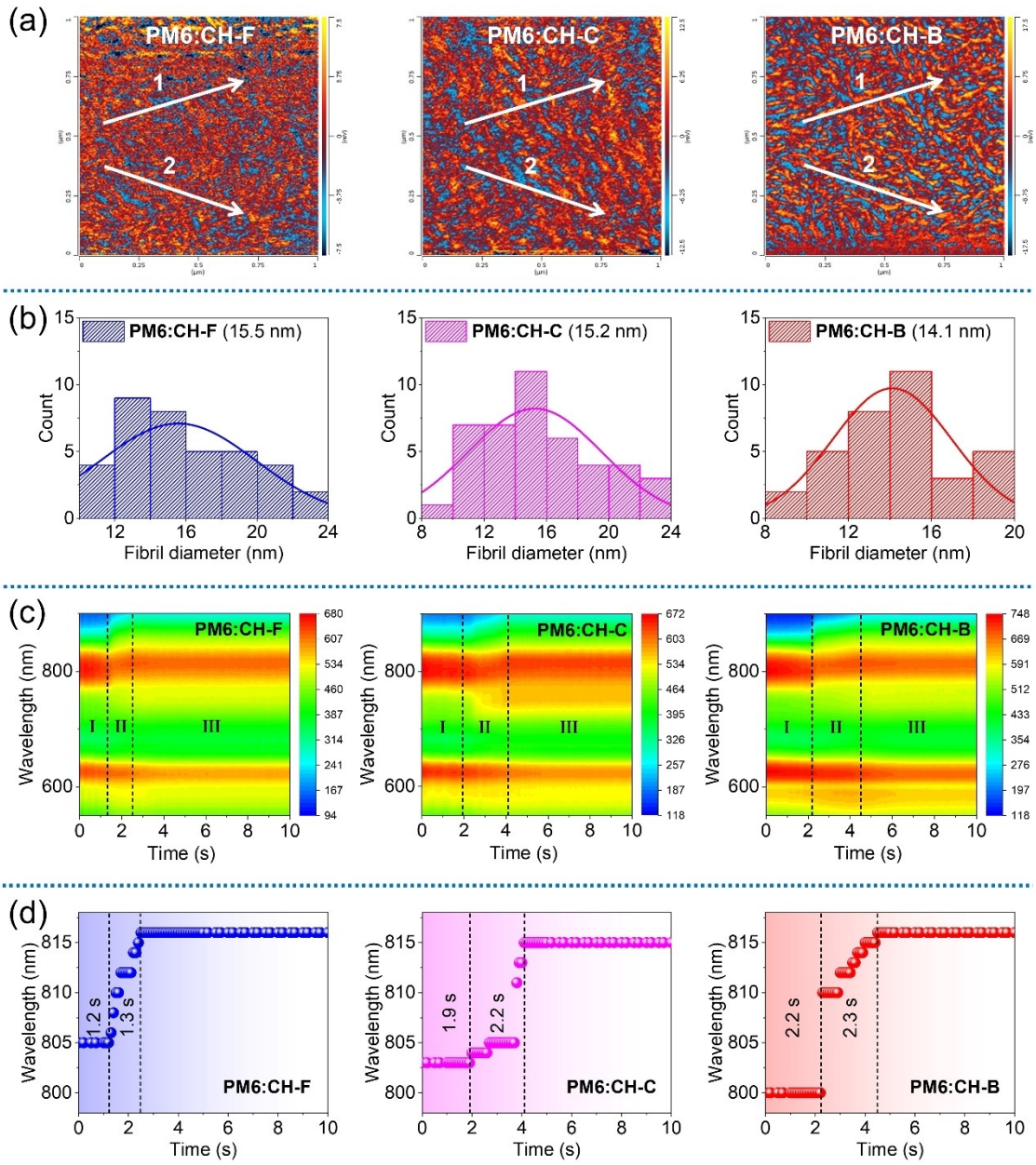

Figure 5. (a) AFM-IR phase images of three blended films by measuring 2216 cm^{-1} signal of acceptors, in which donor and acceptor domains were marked with blue and red colors, respectively. (b) Statistical distribution of phase separation sizes. (c) Color mapping of in situ UV–vis absorption spectra with thermal annealing temperature of 90 °C. (d) The absorption peak wavelength evolution at some representative time points.

microscopy (TEM) images in Figure S21 further verified this fibrillar micromorphology. It has been proven that such a fibrillary morphology could accelerate charge migration and suppress recombination effectively.[24] By further performing a statistical analysis (Figure 5b and S20),[25] a gradually reduced fiber size was afforded, being 15.5, 15.2 and 14.1 nm for PM6:CH–F, PM6:CH–C and PM6:CH–B, respectively. The relatively smaller phase separation for PM6:CH–B could contribute to more efficient exciton dissociation, agreeing well with the discussions in Figure 4d and 4e. Given the D/A phase separation size is closely related to the miscibility between donor and SMAs, the contact angles were measured and corresponding Flory-Huggins interaction parameters (χ) were derived.[26] As shown in Figure S22 and **Table S10**, PM6:CH–B possesses the smallest $\chi_{D:A}$ of 0.05 comparing to that of 0.27 for PM6:CH–F and 0.14 for PM6:CH–C, suggesting the best D/A miscibility for brominating on central units rather than terminals of SMAs. Moreover, GIWAXS analysis of blended films indicated the face-on molecular stacking orientation same as neat films, but with gradually enlarged π–π stacking distances and decreased CCL values from PM6:CH–F, PM6:CH–C to PM6:CH–B (Figure S23 and **Table S11**). The much better D/A miscibility in PM6:CH–B blend should account for its smaller phase separation, enlarged π–π stacking distance and decreased CCL.

As presented in Figure 5c, the in situ UV−vis absorption measurements manifested the different molecular crystallization dynamic in PM6:CH–F, PM6:CH–C and PM6:CH–B blended films, especially for SMA components with the relatively small volume. Typically, the film formation undergoes three stages:[27] (I) Initial stable period at the beginning of thermal annealing. In this stage, both the intensity and position of absorption peaks remain almost unchanged as the solvent gradually evaporates. (II) Rapid transition period. With the continuous solvent evaporation and additive volatilization, the molecule has enough free space to transition from metastable to stable state. This process could be indicated by the considerable redshift of absorption peaks and reflects the movement and rearrangements of SMAs. (III) Micro-variation period under persistent thermal stress. The absorption peak position and intensity maintain overall stability with minor changes, because of the fully evaporation of solvent and additive. As presented in Figure 5d, the absorption peaks markedly red-shift by 11 nm for PM6:CH–F, 12 nm for PM6:CH–C and 16 nm for PM6:CH–B during the rapid transition period. The different degree of absorption peak variation implies the formation of diverse molecular packings during the rapid crystallization of SMAs. Moreover, a gradually prolonged time is needed to reach the micro-variation period from PM6:CH–F (2.5 s), PM6:CH–C (4.1 s) to PM6:CH–B (4.5 s). The relatively slower crystallization process of PM6:CH–B and PM6:CH–C comparing to PM6:CH–F suggests the reinforced D/A interactions, which agrees well with their better D/A miscibility. In short, a delicate and better balance between high crystallization and domain size control has been reached in PM6:CH–B blend through delicately building peripheral F, Cl, Br footprints, which also renders its superior photovoltaic performance comparing to PM6:CH–F and PM6:CH–C. These results highlight the effectiveness of peripheral halogen permutation in delicately tuning photophysical property of SMAs and the resulting photovoltaic performance.

Molecular Packing in Single Crystals

In order to further disclose the influence of peripheral F, Cl, Br footprints on molecular packings, we have grown the single-crystal and acquired the X-ray diffraction analysis for the molecules of CH–F, CH–C and CH–B. Given that the only structural change of SMAs existing in peripheral halogens location, the three isomeric SMAs are expected to maintain the similar and relatively symmetric molecular backbones, which may also contribute to the similar molecular packing modes. The three new single crystals of CH–F, CH–C and CH–B have been deposited in CCDC database with a number of 2372980 for CH–F, 2373250 for CH–C and 2372974 for CH–B. The detailed grown procedures and derived parameters for single crystals were described in Supporting Information and listed in **Table S12** and **S13**.

As presented in Figure S24, all the SMAs illustrated a banana-shaped and helical geometry. As displayed in Figure 6a, both CH–C and CH–B showed much smaller the rectangle-shaped voids of ~19.5×15.5 Å than ~20.7×21.3 Å for CH–F and desired 3D intermolecular packing topological structures. Such a 3D molecular packing network is expected to afford the superior charge dynamic in OSCs.[28] As regards to the intermolecular packing modes (Figure 6b and S25), both CH–C and CH–B mainly possessed three highly similar modes of "end-to-end" (E/E), "end-to-central" (E/C) and "dual central-to-bridge" (dual C/b), however, CH–F show only dual E/C (dual E_{Cl}/b and E_{Br}/b) modes. Because the single crystal of CH–F was grown in a quite different solvent couple from that of CH–C and CH–B, herein we mainly made a detailed comparison between CH–C and CH–B. If we further observe from a more detailed perspective, the three packing modes for CH–C and CH–B above become quite different due to the asymmetric peripheral halogen permutation on SMAs. For example, the "E/E" packing mode of CH–C occurs between two brominated terminals, namely "E_{Br}/E_{Br}". However, "E_F/E_F" packing mode in CH–B is formed by two fluorinated terminals. The similar fashion could be also observed in the other two modes of "E/C" and "dual C/b". Given that the homomorphic F, Cl and Br atoms are featured with gradually enlarged atomic radius (F, 71 pm; Cl, 99 pm; Br, 114 pm) but decreased electronegativity (4.0 for F, 3.0 for Cl and 2.8 for Br), the hyperfine molecular packing structures may also render quite different charge transfer channels and capacities. Therefore, the charge transfer integrals assigned to these three packing modes were evaluated by using DFT calculations. As enumerated in Table S13, the electron transfer integrals for "E/E" packing modes are 25.6 meV for CH–C and 74.7 meV for CH–B; for "E/C" packing modes are 8.8 meV for CH–C and 2.9 meV for CH–B; for "dual C/b" packing modes are 6.9 meV for CH–C and 6.8 meV for CH–B. Obviously, comparing to that of "E_{Br}/E_{Br}" packing mode in CH–C, the significantly enlarged electron transfer integral for "E_F/E_F" packing mode in CH–B should contribute most to the improved charge carrier mobility of CH–B based devices. These interesting findings proved that a desired peripheral halogen footprints on SMAs plays a crucially important role in achieving optimized molecular packing, charge transfer/transport dynamic and photovoltaic performance, etc. In addition, the D/A interface in OSCs is crucially important, although the direct observation methods are still quite lacking. Herein, the PM6:CH–B may possess a stronger interaction and more efficient charge transfer at D/A interface, comparing to that of PM6:CH–F and PM6:CH–C. This was suggested by the better D/A miscibility, smaller phase separation and enlarged π–π stacking distance in PM6:CH–B blends comparing to that of CH–B neat films.

Conclusion

With the aim of delicately tuning the photophysical property of SMAs on the same optimized backbone at both single-molecular and aggregated levels, three highly efficient isomeric SMAs of CH–F, CH–C and CH–B have been

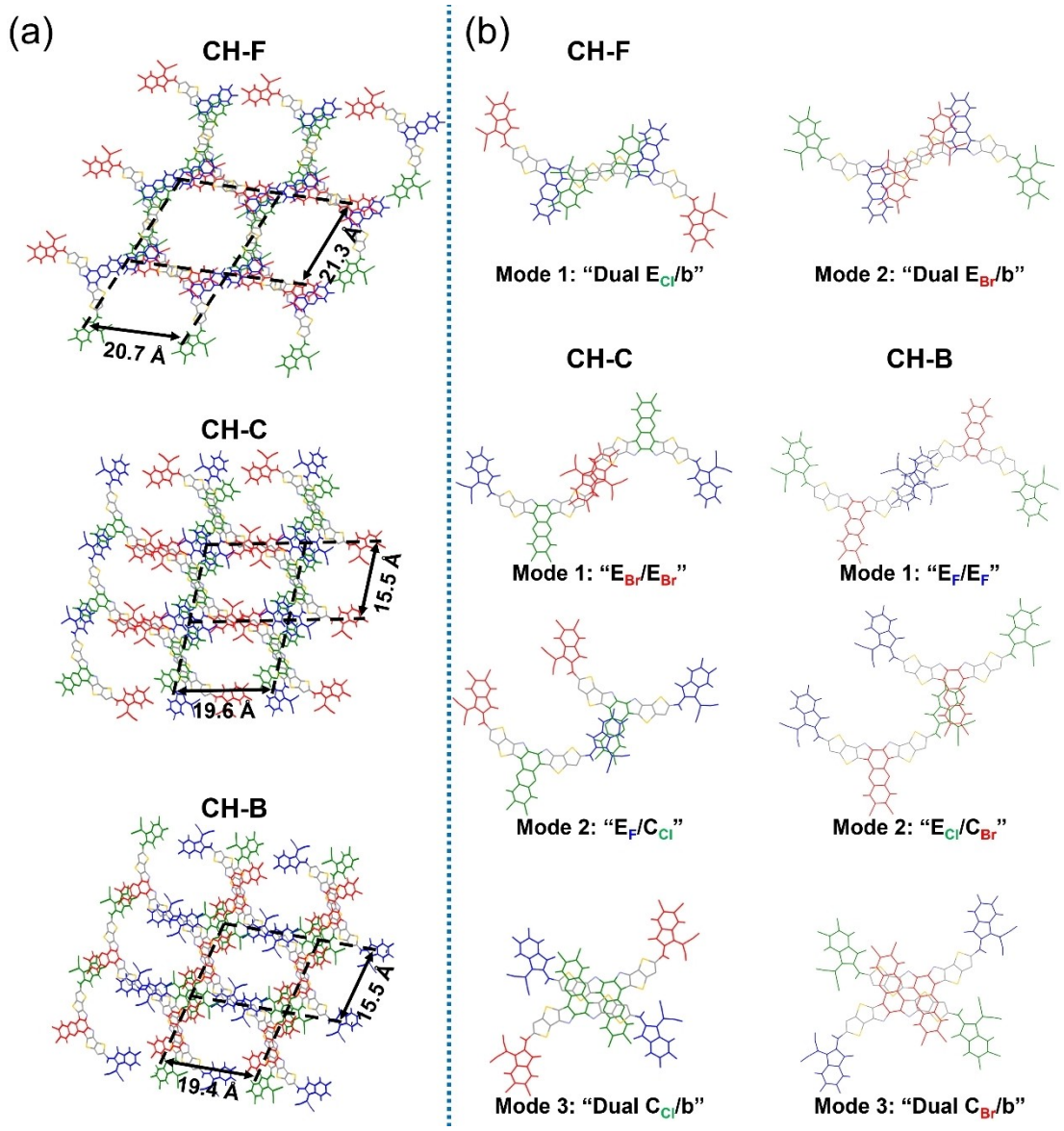

Figure 6. (a) Single-crystal packing topological structures from top view. (b) The main intermolecular packing modes with intermolecular potential over 70 kJ mol^{-1}. Note that the alkyl substitutions on SMAs were omitted for a clearer presentation.

designed and synthesized by rebuilding peripheral F, Cl, Br footprints on a 2D conjugation extended molecular platform. Note that up to eight available halogenation sites could be afforded by such a 2D platform, making it possible to build unique peripheral halogen footprint for each SMAs. Due to the only structural change existing in peripheral halogen locations, all the three SMAs not only maintain an excellent structural symmetry, but also acquire extra asymmetric benefits of enhanced dipole moment and intramolecular charge transfer, etc. A systematic investigation has revealed that central brominating could enhance molecular crystallinity of CH–B without introducing undesirable steric hindrance on end groups. Therefore, a delicate and better balance between high crystallization and domain size control has been reached in PM6:CH–B blend, giving rise to a more suitable fibrillary morphology. Further benefitting from the relatively large ε_r, small E_b, optimized molecular packing and great electron transfer integral of CH–B, PM6:CH–B based binary OSCs afforded the first-class efficiency of 19.78 %, which ranks among the highest PCEs for binary OSCs and significantly outperforms that of 18.55 % for PM6:CH–F and 18.94 % for PM6:CH–C. More excitingly, an efficiency of 18.35 % could be also remained when increasing active layer thickness to ~300 nm, which is the best PCE value for OSCs thus far with thickness up to ~300 nm. Our work highlights the great significance of peripheral halogen footprints on SMAs, thus will stimulate more efforts to explore highly efficient SMAs through delicately peripheral halogen footprints rebuilding using the same optimized backbone.

Supporting Information

The Supporting Information is available free of charge, including materials synthesis, device characterization, NMR and HR-MS spectra (Figure S26–S34), additional tables, *etc.* The synthetic routes to isomerized SMAs (CH–F, CH–C and CH–B) were described in Scheme S1 and the corresponding characterized data/spectra were also illustrated.

Author Contributions

X. C. and P. W. contributed equally to this work. The synthetic works were carried out by P. W.; the device optimizations and measurements were carried out by X. C.; W. Z. and G. L. performed the DFT calculations. Y. C. and Z. Y. conceived and directed the study, revised the manuscript. X. J., H. C., Z. X., J. L., X. B., Y. G., X. W. and C. L. et al. helped to analyze the data and commented on the manuscript.

Acknowledgements

The authors gratefully acknowledge the financial support from Ministry of Science and Technology of the People's Republic of China (National Key R&D Program of China, 2022YFB4200400, 2023YFE0210400, 2019YFA0705900, 2022YFA1203304) and National Natural Science Foundation of China (21935007, 52025033, 52373189, 22204119, 22309090), Natural Science Foundation of Tianjin (23JCZDJC00140, 23JCZDJC01160) and Haihe Laboratory of Sustainable Chemical Transformations. The authors gratefully acknowledge the cooperation of the beamline scientists at BSRF-1W1A beamline.

Conflict of Interest

The authors declare no competing interests.

Data Availability Statement

The data that support the findings of this study are available from the corresponding author upon reasonable request.

Keywords: organic photovoltaic · small molecular acceptor · peripheral halogen permutation · halogenated isomer · molecular packing

[1] a) Y. Lin, J. Wang, Z.-G. Zhang, H. Bai, Y. Li, D. Zhu, X. Zhan, *Adv. Mater.* **2015**, *27*, 1170–1174; b) L. Meng, Y. Zhang, X. Wan, C. Li, X. Zhang, Y. Wang, X. Ke, Z. Xiao, L. Ding, R. Xia, H.-L. Yip, Y. Cao, Y. Chen, *Science* **2018**, *361*, 1094–1098; c) K. Jiang, Q. Wei, J. Y. L. Lai, Z. Peng, H. K. Kim, J. Yuan, L. Ye, H. Ade, Y. Zou, H. Yan, *Joule* **2019**, *3*, 3020–3033; d) J. Yuan, Y. Zhang, L. Zhou, G. Zhang, H.-L. Yip, T.-K. Lau, X. Lu, C. Zhu, H. Peng, P. A. Johnson, M. Leclerc, Y. Cao, J. Ulanski, Y. Li, Y. Zou, *Joule* **2019**, *3*, 1140–1151; e) Z. Zhou, W. Liu, G. Zhou, M. Zhang, D. Qian, J. Zhang, S. Chen, S. Xu, C. Yang, F. Gao, H. Zhu, F. Liu, X. Zhu, *Adv. Mater.* **2019**, *32*, 1906324; f) Y. Cui, H. Yao, J. Zhang, K. Xian, T. Zhang, L. Hong, Y. Wang, Y. Xu, K. Ma, C. An, C. He, Z. Wei, F. Gao, J. Hou, *Adv. Mater.* **2020**, *32*, 1908205; g) C. Li, J. Zhou, J. Song, J. Xu, H. Zhang, X. Zhang, J. Guo, L. Zhu, D. Wei, G. Han, J. Min, Y. Zhang, Z. Xie, Y. Yi, H. Yan, F. Gao, F. Liu, Y. Sun, *Nat. Energy* **2021**, *6*, 605–613; h) Y. Ma, M. Zhang, S. Wan, P. Yin, P. Wang, D. Cai, F. Liu, Q. Zheng, *Joule* **2021**, *5*, 197–209; i) L. Zhu, M. Zhang, J. Xu, C. Li, J. Yan, G. Zhou, W. Zhong, T. Hao, J. Song, X. Xue, Z. Zhou, R. Zeng, H. Zhu, C.-C. Chen, R. C. I. MacKenzie, Y. Zou, J. Nelson, Y. Zhang, Y. Sun, F. Liu, *Nat. Mater.* **2022**, *21*, 656–663; j) Y. Liang, D. Zhang, Z. Wu, T. Jia, L. Lüer, H. Tang, L. Hong, J. Zhang, K. Zhang, C. J. Brabec, N. Li, F. Huang, *Nat. Energy* **2022**, *7*, 1180–1190; k) B. Fan, W. Gao, R. Zhang, W. Kaminsky, F. R. Lin, X. Xia, Q. Fan, Y. Li, Y. An, Y. Wu, M. Liu, X. Lu, W. J. Li, H.-L. Yip, F. Gao, A. K. Y. Jen, *J. Am. Chem. Soc.* **2023**, *145*, 5909–5919; l) L. Wang, C. Chen, Y. Fu, C. Guo, D. Li, J. Cheng, W. Sun, Z. Gan, Y. Sun, B. Zhou, C. Liu, D. Liu, W. Li, T. Wang, *Nat. Energy* **2024**, *9*, 208–218; m) J. Fu, Q. Yang, P. Huang, S. Chung, K. Cho, Z. Kan, H. Liu, X. Lu, Y. Lang, H. Lai, F. He, P. W. K. Fong, S. Lu, Y. Yang, Z. Xiao, G. Li, *Nat. Commun.* **2024**, *15*, 1830; n) Z. Chen, J. Ge, W. Song, X. Tong, H. Liu, X. Yu, J. Li, J. Shi, L. Xie, C. Han, Q. Liu, Z. Ge, *Adv. Mater.* **2024**, *36*, 2406690; o) Y.-J. Xue, Z.-Y. Lai, H.-C. Lu, J.-C. Hong, C.-L. Tsai, C.-L. Huang, K.-H. Huang, C.-F. Lu, Y.-Y. Lai, C.-S. Hsu, J.-M. Lin, J.-W. Chang, S.-Y. Chien, G.-H. Lee, U. S. Jeng, Y.-J. Cheng, *J. Am. Chem. Soc.* **2024**, *146*, 833–848.

[2] a) Y. Shi, Y. Chang, K. Lu, Z. Chen, J. Zhang, Y. Yan, D. Qiu, Y. Liu, M. A. Adil, W. Ma, X. Hao, L. Zhu, Z. Wei, *Nat. Commun.* **2022**, *13*, 3256; b) H. Chen, Y. Zou, H. Liang, T. He, X. Xu, Y. Zhang, Z. Ma, J. Wang, M. Zhang, Q. Li, C. Li, G. Long, X. Wan, Z. Yao, Y. Chen, *Sci. China Chem.* **2022**, *65*, 1362–1373; c) X. Meng, M. Li, K. Jin, L. Zhang, J. Sun, W. Zhang, C. Yi, J. Yang, F. Hao, G.-W. Wang, Z. Xiao, L. Ding, *Angew. Chem. Int. Ed.* **2022**, *61*, e202207762; d) K. Liu, Y. Jiang, G. Ran, F. Liu, W. Zhang, X. Zhu, *Joule* **2024**, *8*, 1–17; e) Z. Wang, M. Ji, A. Tang, M. Du, C. Mu, Y. Liu, E. Wang, E. Zhou, *Energy Environ. Sci.* **2024**, *17*, 3868–3877; f) Z. Luo, W. Wei, R. Ma, G. Ran, M. H. Jee, Z. Chen, Y. Li, W. Zhang, H. Y. Woo, C. Yang, *Adv. Mater.* **2024**, *36*, 2407517.

[3] a) H. Chen, H. Liang, Z. Guo, Y. Zhu, Z. Zhang, Z. Li, X. Cao, H. Wang, W. Feng, Y. Zou, L. Meng, X. Xu, B. Kan, C. Li, Z. Yao, X. Wan, Z. Ma, Y. Chen, *Angew. Chem. Int. Ed.* **2022**, *61*; b) T. Xu, Z. Luo, R. Ma, Z. Chen, T. A. Dela Peña, H. Liu, Q. Wei, M. Li, C. e. Zhang, J. Wu, X. Lu, G. Li, C. Yang, *Angew. Chem. Int. Ed.* **2023**, *62*, e202304127.

[4] a) T. J. Aldrich, M. Matta, W. Zhu, S. M. Swick, C. L. Stern, G. C. Schatz, A. Facchetti, F. S. Melkonyan, T. J. Marks, *J. Am. Chem. Soc.* **2019**, *141*, 3274–3287; b) L. Yan, H. Zhang, Q. An, M. Jiang, A. Mahmood, M. H. Jee, H. R. Bai, H. F. Zhi, S. Zhang, H. Y. Woo, J. L. Wang, *Angew. Chem. Int. Ed.* **2022**, *61*, e202209454 ; c) X. Gu, R. Zeng, Y. Hou, N. Yu, J. Qiao, H. Li, Y. Wei, T. He, J. Zhu, J. Deng, S. Tan, C. e. Zhang, Y. Cai, G. Long, X. Hao, Z. Tang, F. Liu, X. Zhang, H. Huang, *Angew. Chem. Int. Ed.* **2024**, *63*, e202407355.

[5] a) L. Zhu, J. Zhang, Y. Guo, C. Yang, Y. Yi, Z. Wei, *Angew. Chem. Int. Ed.* **2021**, *60*, 15348–15353; b) H. Liang, X. Bi, H. Chen, T. He, Y. Lin, Y. Zhang, K. Ma, W. Feng, Z. Ma, G. Long, C. Li, B. Kan, H. Zhang, O. A. Rakitin, X. Wan, Z. Yao, Y. Chen, *Nat. Commun.* **2023**, *14*, 4707.

[6] a) Z. Yao, X. Cao, X. Bi, T. He, Y. Li, X. Jia, H. Liang, Y. Guo, G. Long, B. Kan, C. Li, X. Wan, Y. Chen, *Angew. Chem.*

Int. Ed. **2023**, *62*, e202312630; b) J. Chen, D. Li, M. Su, Y. Xiao, H. Chen, M. Lin, X. Qiao, L. Dang, X.-C. Huang, F. He, Q. Wu, *Angew. Chem. Int. Ed.* **2023**, *62*, e202215930; c) D.-L. Ma, Q.-Q. Zhang, C.-Z. Li, *Angew. Chem. Int. Ed.* **2023**, *62*, e202214931; d) Y. Sun, L. Wang, C. Guo, J. Xiao, C. Liu, C. Chen, W. Xia, Z. Gan, J. Cheng, J. Zhou, Z. Chen, J. Zhou, D. Liu, T. Wang, W. Li, *J. Am. Chem. Soc.* **2024**, *146*, 12011–12019.

[7] a) C. Sun, S. Qin, R. Wang, S. Chen, F. Pan, B. Qiu, Z. Shang, L. Meng, C. Zhang, M. Xiao, C. Yang, Y. Li, *J. Am. Chem. Soc.* **2020**, *142*, 1465–1474; b) Z. Chen, S. Zhang, T. Zhang, J. Ren, J. Dai, H. Li, J. Qiao, X. Hao, J. Hou, *Angew. Chem. Int. Ed.* **2024**, *63*, e202317892.

[8] Z. Yao, X. Wan, C. Li, Y. Chen, *Acc. Mater. Res.* **2023**, *4*, 772–785.

[9] a) L. Wang, Q. An, L. Yan, H.-R. Bai, M. Jiang, A. Mahmood, C. Yang, H. Zhi, J.-L. Wang, *Energy Environ. Sci.* **2022**, *15*, 320–333; b) T. Chen, S. Li, Y. Li, Z. Chen, H. Wu, Y. Lin, Y. Gao, M. Wang, G. Ding, J. Min, Z. Ma, H. Zhu, L. Zuo, H. Chen, *Adv. Mater.* **2023**, *35*, 2300400; c) M. Deng, X. Xu, Y. Duan, W. Qiu, L. Yu, R. Li, Q. Peng, *Adv. Mater.* **2024**, *36*, 2308216.

[10] X. Wan, C. Li, M. Zhang, Y. Chen, *Chem. Soc. Rev.* **2020**, *49*, 2828–2842.

[11] a) X. Zhu, G. Zhang, J. Zhang, H.-L. Yip, B. Hu, *Joule* **2020**, *4*, 2443–2457; b) C. He, Q. Shen, B. Wu, Y. Gao, S. Li, J. Min, W. Ma, L. Zuo, H. Chen, *Adv. Energy Mater.* **2023**, *13*, 2204154.

[12] J. Gao, H. Bai, P. Li, Y. Zhou, W. Su, C. Liu, X. Li, Y. Wu, B. Hu, Z. Liang, Z. Bi, X. Li, L. Yan, H. Du, G. Lu, C. Gao, K. Wang, Y. Liu, W. Ma, Q. Fan, *Adv. Sci.* **2024**, *11*, 2403334.

[13] H. Hu, M. Ghasemi, Z. Peng, J. Zhang, J. J. Rech, W. You, H. Yan, H. Ade, *Adv. Mater.* **2020**, *32*, 2005348.

[14] a) P. Müller-Buschbaum, *Adv. Mater.* **2014**, *26*, 7692–7709; b) Y. Wu, Q. Hu, P. Fan, Y. Jiang, W. Zhong, W. Hu, T. P. Russell, *J. Phys. Chem. C* **2021**, *125*, 15863–15871.

[15] X. Cao, J. Guo, Z. Li, X. Bi, H. Liang, Z. Xiao, Y. Guo, X. Jia, Z. Xu, K. Ma, Z. Yao, B. Kan, X. Wan, C. Li, Y. Chen, *ACS Energy Lett.* **2023**, *8*, 3494–3503.

[16] a) L. Zhu, J. Zhang, Y. Guo, C. Yang, Y. Yi, Z. Wei, *Angew. Chem. Int. Ed.* **2021**, *60*, 15348–15353; b) J. Ji, L. Zhu, X. Xiong, F. Liu, Z. Liang, *Adv. Sci.* **2022**, *9*, 2200864.

[17] a) J. Benduhn, K. Tvingstedt, F. Piersimoni, S. Ullbrich, Y. Fan, M. Tropiano, K. A. McGarry, O. Zeika, M. K. Riede, C. J. Douglas, S. Barlow, S. R. Marder, D. Neher, D. Spoltore, K. Vandewal, *Nat. Energy* **2017**, *2*, 17053; b) F. D. Eisner, M. Azzouzi, Z. Fei, X. Hou, T. D. Anthopoulos, T. J. S. Dennis, M. Heeney, J. Nelson, *J. Am. Chem. Soc.* **2019**, *141*, 6362–6374.

[18] M. Zhang, X. Guo, W. Ma, H. Ade, J. Hou, *Adv. Mater.* **2015**, *27*, 4655–4660.

[19] L. J. A. Koster, V. D. Mihailetchi, R. Ramaker, P. W. M. Blom, *Appl. Phys. Lett.* **2005**, *86*, 123509.

[20] X. Zhang, C. Li, J. Xu, R. Wang, J. Song, H. Zhang, Y. Li, Y.-N. Jing, S. Li, G. Wu, J. Zhou, X. Li, Y. Zhang, X. Li, J. Zhang, C. Zhang, H. Zhou, Y. Sun, Y. Zhang, *Joule* **2022**, *6*, 444–457.

[21] a) L. Zhan, S. Yin, Y. Li, S. Li, T. Chen, R. Sun, J. Min, G. Zhou, H. Zhu, Y. Chen, J. Fang, C. Q. Ma, X. Xia, X. Lu, H. Qiu, W. Fu, H. Chen, *Adv. Mater.* **2022**, *34*, 2206269; b) Y. Wei, Y. Cai, X. Gu, G. Yao, Z. Fu, Y. Zhu, J. Yang, J. Dai, J. Zhang, X. Zhang, X. Hao, G. Lu, Z. Tang, Q. Peng, C. Zhang, H. Huang, *Adv. Mater.* **2023**, *36*, 2304225.

[22] a) X. Lu, C. Xie, Y. Liu, H. Zheng, K. Feng, Z. Xiong, W. Wei, Y. Zhou, *Nat. Energy* **2024**, *9*, 793–802; b) H. Chen, W. Sun, R. Zhang, Y. Huang, B. Zhang, G. Zeng, J. Ding, W. Chen, F. Gao, Y. Li, Y. Li, *Adv. Mater.* **2024**, *36*, 2402350.

[23] J. Song, C. Li, H. Ma, B. Han, Q. Wang, X. Wang, D. Wei, L. Bu, R. Yang, H. Yan, Y. Sun, *Adv. Mater.* **2024**, *36*, 2406922.

[24] F. Zhao, C. Wang, X. Zhan, *Adv. Energy Mater.* **2018**, *8*, 1703147.

[25] Z. Chen, J. Zhu, D. Yang, W. Song, J. Shi, J. Ge, Y. Guo, X. Tong, F. Chen, Z. Ge, *Energy Environ. Sci.* **2023**, *16*, 3119–3127.

[26] S. Nilsson, A. Bernasik, A. Budkowski, E. Moons, *Macromolecules* **2007**, *40*, 8291–8301.

[27] J. Song, Y. Li, Y. Cai, R. Zhang, S. Wang, J. Xin, L. Han, D. Wei, W. Ma, F. Gao, Y. Sun, *Matter* **2022**, *5*, 4047–4059.

[28] W. Zhu, A. P. Spencer, S. Mukherjee, J. M. Alzola, V. K. Sangwan, S. H. Amsterdam, S. M. Swick, L. O. Jones, M. C. Heiber, A. A. Herzing, G. Li, C. L. Stern, D. M. DeLongchamp, K. L. Kohlstedt, M. C. Hersam, G. C. Schatz, M. R. Wasielewski, L. X. Chen, A. Facchetti, T. J. Marks, *J. Am. Chem. Soc.* **2020**, *142*, 14532–14547.

Manuscript received: September 8, 2024
Accepted manuscript online: November 8, 2024
Version of record online: ■■, ■■

Research Article

Organic Solar Cells

X. Cao, P. Wang, X. Jia, W. Zhao, H. Chen, Z. Xiao, J. Li, X. Bi, Z. Yao,* Y. Guo, G. Long, C. Li, X. Wan, Y. Chen* e202417244

Rebuilding Peripheral F, Cl, Br Footprints on Acceptors Enables Binary Organic Photovoltaic Efficiency Exceeding 19.7%

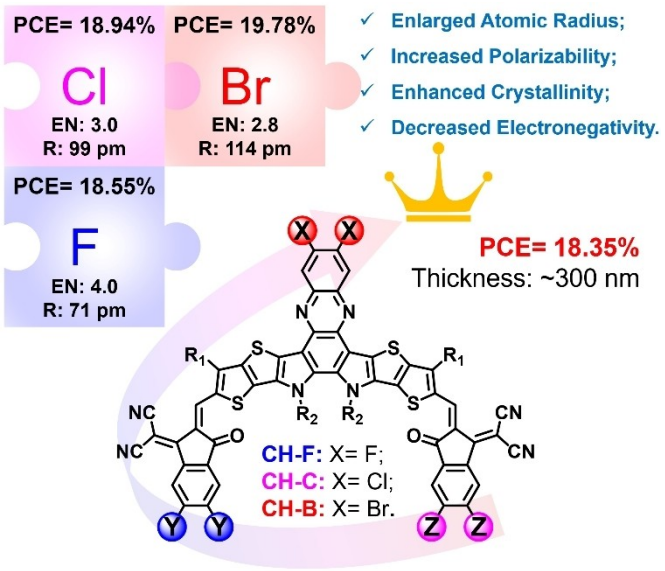

Rebuilding Peripheral F, Cl, Br Footprints

By delicately rebuilding peripheral F, Cl, Br footprints, the central brominated acceptor of CH–B afforded the first-class efficiency of 19.78% for binary organic solar cells, also achieved the best performance when further increasing active layer thickness to ~300 nm.